# Design Study of a Low Field Dipole for the FCC-Ee Booster Ring

Halil Deveci, L. von Freeden, M. Pentella, and C. Petrone

***Abstract*—The FCC-ee booster dipoles are low-field iron-dominated cycled H-type magnets. They consist of an 11-meter-long laminated steel yoke with anodized aluminium busbars instead of coils. The magnet is required to operate at fields down to 6.5 mT for 20Ge V injection. At such low field levels parasitic effects become significant, for example, the Earth's magnetic field, yoke hysteresis, and stray fields from cables. This poses a unique set of design challenges that are answered in this paper. The hysteretic effect is modelled, and the cross-section of the magnet is optimised to obtain the required field quality across the full cycle from 6.5 mT to 59 mT. The predictive power of the hysteresis model is validated by the test of a similar magnet from CERN stock. Finally, magnetic measurements from a short prototype magnet are reported. The test results confirm that the proposed magnet meets the design requirements, demonstrating the feasibility of dipoles for 20Ge V booster injection energy.**

***Index Terms*—Hysteresis, accelerator dipoles, magnet design and analysis techniques, electromagnets, electromagnetic measurements.**

## I. Introduction

THE 2020 European strategy for particle physics identified the Future Circular Collider (FCC) project as the preferred option for a next-generation collider at CERN [1]. The FCC project envisions the construction of a new tunnel with a circumference of 90.7 km, an average depth of 200 m, and four experimental caverns. Utilisation of this tunnel will occur in two distinct phases. In the first phase, FCC-ee, a normal-conducting electron–positron collider will be installed for precision measurements. In the second phase, FCC-hh, a superconducting hadron–hadron collider will be implemented to explore the high-energy frontier.

During the FCC-ee phase, the tunnel will host two machines: the collider and the booster. The booster will accelerate the beams from an injection energy of 20Ge V up to the operating energy of the collider and provide continuous top-up injection. The collider will operate at four different beam energies, corresponding to the processes under study: Z boson production (45.6Ge V), W boson production (80Ge V), associated ZH production (120Ge V), and $t\bar{t}$ pair production (182.5Ge V) [2].

Received 28 July 2025; revised 25 September 2025; accepted 26 September 2025. Date of publication 7 October 2025; date of current version 17 October 2025. *(Corresponding author: Halil Deveci.)*

Halil Deveci is with the CERN, Technology Department, 1211 Geneva, Switzerland (e-mail: halil.deveci@cern.ch).

L. von Freeden, M. Pentella, and C. Petrone are with the CERN, Technology Department, Magnets Superconductors and Cryostats Group, 1211 Geneva, Switzerland (e-mail: luke.von.freeden@cern.ch; mariano.pentella@cern.ch; carlo.petrone@cern.ch).

Color versions of one or more figures in this article are available at https://doi.org/10.1109/TASC.2025.3618594.

Digital Object Identifier 10.1109/TASC.2025.3618594

TABLE I
Magnet Requirements, FODO Version 24

| Parameter | Units | Value |
|---|---|---|
| Total number of dipoles in lattice | | 6176 |
| ... of which in arcs | | 5536 |
| Pole gap | mm | 65.0 |
| Magnetic length | m | 11.0 |
| Max field ($t\bar{t}$ extraction, 182.5 GeV) | mT | 58.9 |
| Min field (injection, 20 GeV) | mT | 6.5 |
| Good field region (GFR) | mm | ⌀20 |
| Relative field distortion in GFR | | $1 \times 10^{-4}$ |
| Magnet-to-magnet integral field deviation | | $1 \times 10^{-3}$ |

TABLE II
Comparison of the FCC-Ee Booster, CEPC Booster, LHeC, and LEP Dipole Parameters

| Machine | Minimum field (mT) | Ratio peak / min field |
|---|---|---|
| FCC-ee booster | 6.5 | 9.0 |
| CEPC booster | 9.5 | 6.0 |
| LEP | 21.5 | 6.3 |
| LHeC ring-ring | 12.7 | 6.0 |

The requirements for the FCC-ee booster dipole are summarised in Table I. The parameters correspond to version 24 of the booster optics, which was the baseline for the feasibility study report [2]. Among the four operation cycles, the $t\bar{t}$ cycle is the most challenging for the magnet design. The $t\bar{t}$ cycle has the largest field range, implying the highest remanent magnetisation in the yoke. The requirements for the FCC-ee booster dipoles are beyond those previously set for cycled low-field dipoles both in terms of minimum field and dynamic range. A comparison of the key parameters of the FCC-ee booster dipoles with those of the Chinese Electron Positron Collider (CEPC) booster [3], the Large Electron Position (LEP) collider [4], and the ring-ring option Large Hadron electron Collider (LHeC) [5] is provided in Table II.

## II. Design of the Magnet

The proposed design is an H-shape dipole with directly cooled aluminium busbars. A cross section of the design is shown in Fig. 1 and its parameters are presented in Table III. This section will discuss the design choices made.

During the pre-study three design topologies, C-shape, O-shape, and H-shape, were compared to assess the suitability to

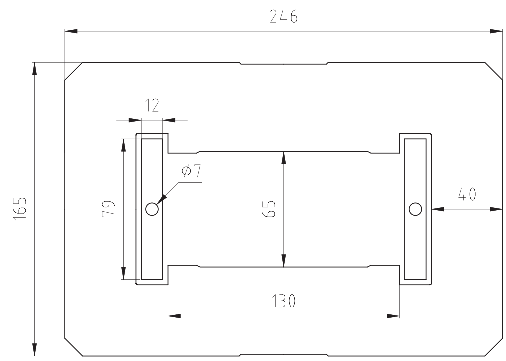


Fig. 1. Cross section of the proposed FCC-ee booster dipole magnet for v24 optics.

TABLE III
PARAMETERS OF THE FCC-EE BOOSTER DIPOLE MAGNET FOR V24 OPTICS

| Parameter | Units | Value |
|---|---|---|
| Peak current | A | 3065 |
| Resistance | mΩ | 0.7 |
| Inductance | μH | 44 |
| Peak voltage, magnet | V | 2.2 |
| Conductor, Aluminium | mm | 12 × 79, ⌀7 |
| Number of turns | | 1 |
| RMS current density, $t\bar{t}$ | A mm$^{-2}$ | 1.35 |
| Yoke mass | kg | 2398 |
| Conductor mass | kg | 54 |
| Pressure drop | bar | 2 |
| Cooling flow | L min$^{-1}$ | 4.75 |
| Maximum temperature rise | °C | 5 |

TABLE IV
COMPUTED SHIELDING FACTORS OF THE THREE TOPOLOGIES CONSIDERED AND EARTH'S MAGNETIC FIELD IN GENEVA

| | Horizontal | Vertical |
|---|---|---|
| Shielding factor O-shape and H-shape | 400 | 65 |
| Shielding factor C-shape | 10 | 30 |
| Earth's magnetic field | 22.3 μT | 42.3 μT |

achieve the required field quality. The shielding performance of candidate designs was computed with only background fields present. The results were compared using the shielding factor, given by

$$f_s = \frac{B_o}{B_i} \tag{1}$$

where $B_o$ is the background field and $B_i$ is the field at the centre of the magnet. The results of this study are presented in Table IV. The vertical and horizontal planes are considered separately. The angle between horizontal component of the Earth's magnetic field and the magnets varies around the ring. The vertical component of the Earth's magnetic field is similar at all positions around the ring. However, the Earth's field can be locally distorted by ferromagnetic materials and there are other sources of background fields in the tunnel e.g. from cables. The C-shape topology does not provide sufficient shielding. For example, in the horizontal plane the Earth's field is only reduced to $3.4 \times 10^{-4}$ of main field at injection. Consequently, the C-shape topology was rejected. Between the remaining options, the H-shape topology was chosen over the O-shape topology because its pole geometry can be more effectively shaped to maintain field quality across the full excitation cycle in the presence of yoke magnetisation effects.

Having selected an H-shape, the pole shape was optimised for field quality across the cycle. Additional material or "shims" are used at the horizontal extremities of the pole to compensate negative sextupolar errors arising from the truncation of the ideal, infinite, pole. The final width of the pole is 130 mm, or equivalently a 55 mm overhang either side of the GFR. In literature, formulae are provided for the pole overhang as a function of normalised field quality and aperture for both a flat pole and an optimally shimmed pole [6]. For our parameters, the formulae give 79 mm for a flat pole and 34 mm for an optimally shimmed pole. The additional pole overhang was required to ensure the field quality in the presence of yoke magnetisation.

In a dipole, the required magnetomotive force (MMF) is given by

$$NI = \frac{Bg}{\mu_0 \eta} \tag{2}$$

where $B$ is the dipole field, $g$ is the aperture height, $\mu_0$ is the permeability of free space, and $\eta$ is the magnetic efficiency. After FEA studies, 3065 A are required for 58.9 mT, corresponding to $\eta = 0.99$.

The excitation is applied using aluminium busbars which are cheaper than copper coils. The labour cost of coil winding and impregnation is avoided completely and the material cost is 85% lower for the same joule loss. The root mean squared (RMS) current density in the busbars is very low, 1.35 $\text{Amm}^{-2}$ for the $t\bar{t}$ cycle, to optimise the lifetime cost of the magnets. Despite the low current density, the busbars are directly cooled to avoid excessive heating of the air in the tunnel. The busbars allow the magnets to be connected end-to-end, which minimises transmission losses.

The back leg has a thickness of 40 mm, thicker than necessary for mechanical stability and flux return. The back leg is oversized for two reasons. Firstly, a lower peak field results in less magnetisation in the yoke, improving the performance at low field. Secondly, the additional material shields the tunnel from synchrotron radiation and may avoid the need for a dedicated shielding system [2, Sec. 4.3].

The final material choice for the yoke is still under study to optimise the cost and performance trade-offs implied by lamination thickness and steel grade. For the time being, M270-50 A is taken as the baseline due to its commercial availability and magnetic softness.

## III. MODELLING OF HYSTERESIS

ANSYS Maxwell [7] was used to model the hysteretic effects in the proposed design during the $t\bar{t}$ cycle: ramping from 6.5 mT to 58.9 mT in 2.03 s, a 90 ms flat-top, and a symmetric ramp down. In ANSYS Maxwell, hysteresis loops are extrapolated using the virgin curve and a single value of coercivity. The material data used in this study were taken from Epstein frame

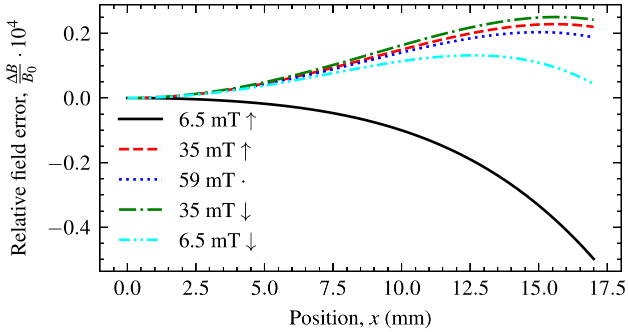


Fig. 2. Computed 2D magnetic field error on the central axis of the proposed magnet during one complete cycle from a degaussed state. ↑ indicates ramp-up, · flat-top, and ↓ ramp-down.

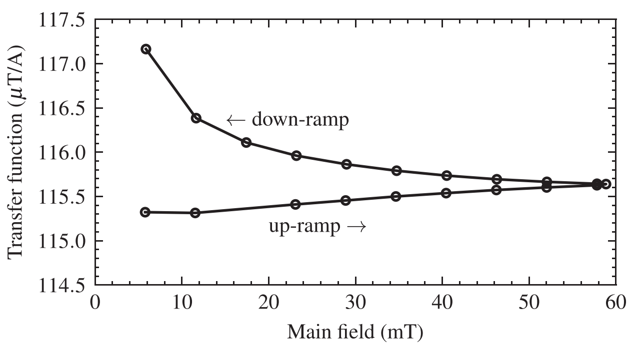


Fig. 3. Computed 2D transfer function of the proposed magnet during one complete cycle from a degaussed state. The cycle starts at (6.5 mT, 115.4$\mu$T A$^{-1}$).

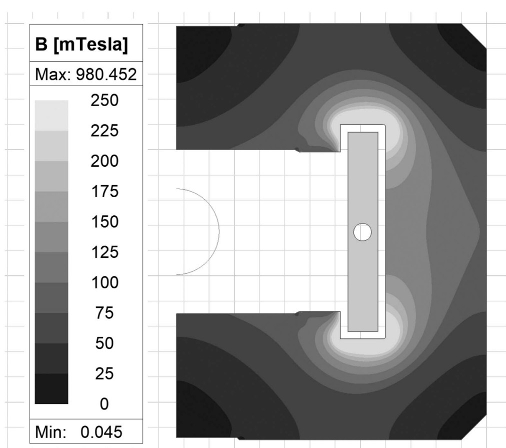


Fig. 4. Computed 2D field of the proposed magnet at extraction.

measurements conducted by the steel manufacturer. The coercivity value was set to 15 Am$^{-1}$, which corresponds to the average flux density in the back leg. The shims were adjusted to optimise the field quality across the full cycle. The computed field error of the proposed design is shown in Fig. 2, and the computed transfer function in Fig. 3. The field distribution in the yoke is shown in Fig. 4.

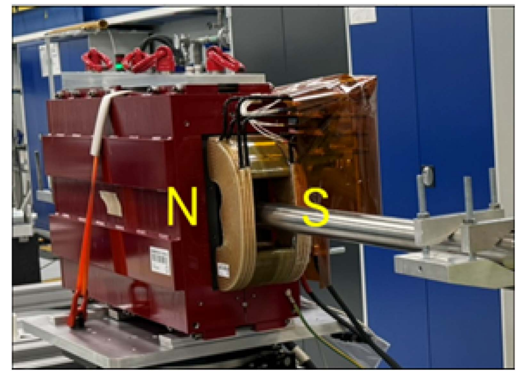


Fig. 5. Test set-up used to measure the T-BV1 type magnet from CERN stock.

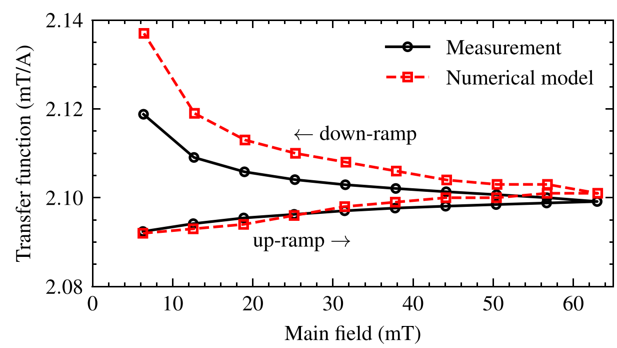


Fig. 6. Comparison of the computed and measured transfer function of the T-BV1 type magnet during one cycle from a degaussed state. The cycles start at (6.5 mT, 2.09 mTA$^{-1}$).

### *A. Validation of Model Using T-BV1*

Before construction of a prototype, the modelling approach was validated by measuring a T-BV1 type magnet from CERN stock. The magnet was first degaussed and then sequentially stepped through the $t\bar{t}$ cycle in a quasi-static test regime. The magnetic field was measured using a 37 mm diameter rotating coil placed in the central flat field region of the magnet. The test set-up is shown in Fig. 5. The transfer function measured is compared with the modelled result in Fig. 6. The model over-predicts the transfer function by only 1%, which is remarkably accurate.

## IV. Short Prototype Magnet

To validate the proposed design, a short prototype magnet has been built and measured. Laser cut laminations of M270-50 A were stacked to a length of 500 mm with two 15 mm thick non-magnetic end plates. The stack was cured and then bars were welded to the external faces to restrain the stack. The pole faces and reference surfaces were then machined to their final shape. The magnet was then pinned, assembled with a coil, and bolted closed. Coils were used as a proxy for the busbars for practicality. The final yoke is sufficiently long to ensure a flat field region in the centre for measurement. An image of the finished prototype magnet is shown in Fig. 7.

The central field of the magnet was measured using a 37 mm diameter rotating coil placed in the central flat field region of the

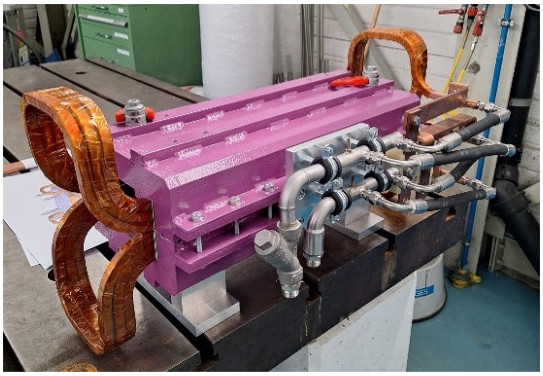

Fig. 7. Short prototype magnet built and tested to verify the proposed design.

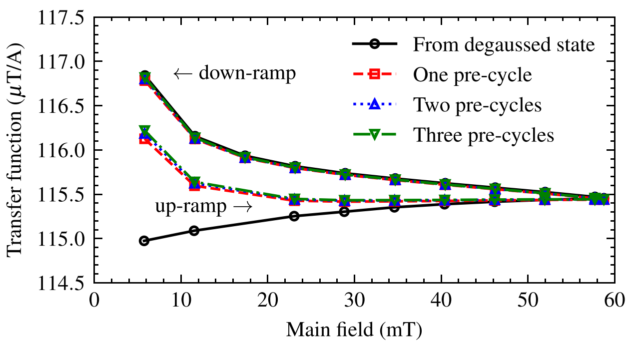


Fig. 8. Measured transfer function of the short prototype magnet from degaussed state and after one, two, and three pre-cycles. The cycle from degaussed state starts at (6.5 mT, $115\mu\mathrm{T\,A}^{-1}$). The cycles for the pre-cycled cases start around (6.5 mT, 116.3 $\mu\mathrm{T\,A}^{-1}$).

magnet. Before each measurement, the magnet was degaussed. The magnet was then subjected to either zero, one, two, three pre-cycles from injection field to extraction field and back. The magnet was then sequentially stepped through the $\mathrm{t\bar{t}}$ cycle in a quasi-static test regime. The magnetic measurements are corrected for background field using a measurement made directly after the degaussing step.

The measured transfer function is shown in Fig. 8. After two pre-cycles the transfer function of the magnet stabilised with $3.4 \times 10^{-4}$ relative change in transfer function at injection between the two pre-cycle and three pre-cycle cases. Comparing the transfer function at injection of the degaussed and pre-cycled cases, we can estimate that at injection the remanent magnetisation contributes 60 $\mu$T or around 1% of the main field. We can therefore conclude that the coercivity of the steel must be controlled to better than 10% to achieve the required $1 \times 10^{-3}$ magnet-to-magnet relative field error. This constraint can be achieved with typical electrical steels [8]. This is a useful result to establish the feasibility of the low field dipole, noting that it must be interpreted with consideration to all sources of variation. The final magnetic length of a magnet can be adjusted by adding or removing material at the ends after production. However, variations in steel properties lead to magnet-to-magnet relative field error that changes with main field rendering this approach less effective. Comparing the measured transfer function with that predicted by modelling we again see agreement within 1%.

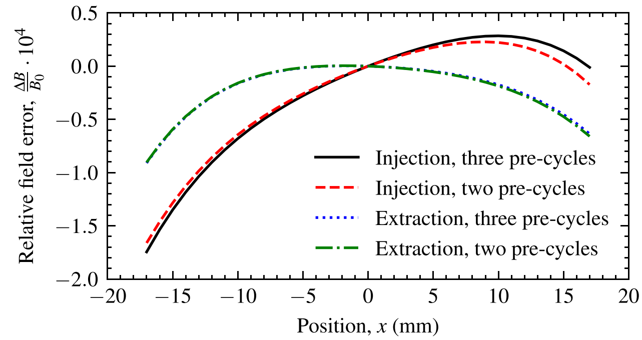


Fig. 9. Measured relative field error on axis of the baseline short prototype magnet at injection, 6.5 mT, and extraction, 58.9 mT for the two pre-cycle and three pre-cycle cases.

The measured relative field error on axis at injection and extraction for the two pre-cycle and three pre-cycle cases is shown in Fig. 9. We see less than $\pm 1 \times 10^{-4}$ relative field error in the GFR in all measurements and less than $1 \times 10^{-5}$ change in relative field error between cycles.

The measured sextupolar error is constant within $3 \times 10^{-6}$ throughout the cycle, contributing a relative field error at the extremities of the GFR ranging from $-0.15 \times 10^{-4}$ at injection to $-0.12 \times 10^{-4}$ at extraction. The numerical model predicts a positive sextupolar error, implying that the shims are less effective than expected. It is hypothesised that this is due to a local material degradation in the shims due to the laser cutting process. Follow-up permeameter testing on thin laser cut samples showed a nearly seven fold reduction in relative permeability with respect to virgin samples [9].

At injection, we see a quadrupolar component contributing $\pm 0.5 \times 10^{-4}$ relative field error at the extremities of the GFR which decays at extraction. This implies a constant left-right asymmetry in the magnetisation of the yoke which becomes relatively less significant as the main field increases. The laminations were stacked in an alternating orientation, with groups rotated 180○ about the vertical symmetry axis. This reduces the likelihood that material asymmetry is the cause. In the baseline design, the terminal busbars run parallel to the yoke for around 12 cm from one end of the magnet. It was hypothesised these terminal busbars could induce the observed asymmetric magnetisation. The busbars were reconfigured to exit perpendicularly at the end of the yoke, the measured field remained unchanged. This rules out the terminal busbars as the cause, leaving the asymmetry unexplained and subject to future investigation.

A second prototype is underway to further investigate the observed effects and support ongoing design refinements.

## V. Conclusion

A dipole magnet design has been proposed that meets the requirements of the v24 FCC-ee booster optics. A modelling approach has been developed that can accurately predict the transfer function of low field magnets, including yoke magnetisation. A short prototype magnet was built and tested. The results demonstrate that the requirements for field range, field quality, and repeatability are technically achievable. Further prototyping and design optimisation are underway as part of the FCC-ee technical design phase.


## ACKNOWLEDGMENT

The authors would like to thank A. Milanese and D. Schoerling for many insightful discussions, the teams in the TE-MSC laboratories for their support building and measuring the prototype, and our colleagues of the FCC feasibility study for the fruitful collaboration.


## REFERENCES


[1] "2020 update of the European strategy for particle physics (Brochure)," Geneva, Switzerland, Tech. Rep. CERN-ESU-015, 2020.[Online]. Available: https://cds.cern.ch/record/2721370

[2] M. Benedikt et al., "Future circular collider feasibility study report volume 2 : Accelerators, technical infrastructure and safety," CERN, Geneva, Tech. Rep. CERN-FCC-ACC-2025-0004, 2025. [Online]. Available: http://cds.cern.ch/record/2928793

[3] J. Gao et al., "CEPC technical design report: Accelerator," *Radiat. Detection Techn. Methods*, vol. 8, no. 1, pp. 429–440, 2024.

[4] "LEP design report: Vol. 2, the LEP main ring," CERN, Geneva, Tech. Rep. CERN-LEP-84-01, 1984. [Online]. Available: https://cds.cern.ch/record/102083

[5] D. Tommasini, M. Buzio, and R. Chritin, "Dipole magnets for the LHeC ring-ring option," *IEEE Trans. Appl. Supercond.*, vol. 22, no. 3, pp. 4000203–4000203, Jun. 2012.

[6] J. T. Tanabe, *Iron Domindated Electromagnets: Design, Fabrication, Assembly and Measurements*, Stanford, USA: World Scientific Publishing, 2005.

[7] ANSYS Maxwell, Release 2022 R2, ANSYS, Inc., Canonsburg, PA, USA, preisach hysteresis model, 2022. [Online]. Available: https://www.ansys.com/products/electronics/ansys-maxwell

[8] M. Pentella, "Characterization of magnetic materials at extreme ranges of field, temperature, and permeability," Ph.D. dissertation, Politecnico di Torino, Turin, Italy, 2022.

[9] M. Pentella, "Magnetic measurement of two FeSi steel grades for the FCC-ee booster dipole magnets," CERN, Internal Rep. EDMS 3199957, 2025.